Supplementary Information:

Optical-resolution functional gastrointestinal photoacoustic endoscopy based on optical heterodyne detection of ultrasound

Liang et al.

Supplementary Note S1: Noise of the ultrasound sensing system

Figure S1a shows a schematic of ultrasound sensing system. The sensing element is a laser cavity confined by two Bragg gratings fabricated in a rare-earth-doped fiber. The cavity has a single-longitudinal-mode laser output with both *x*- and *y*-polarizations when pumped with a 980-nm semiconductor laser through a wavelength-division multiplexer (WDM). The orthogonal laser beams have slightly different lasing frequencies due to the intrinsic birefringence. Figure S1b exhibits the measured optical spectrum of the laser output with a frequency resolution of 10 MHz (optical spectrum analyzer: BOSA 200 CL, Aragon Photonics Labs), which shows a $\omega_b = 2\pi \times 1.74$ GHz frequency spacing. An optical isolator is used to prevent unwanted optical scattering or endface reflections into the cavity. The *x*- and *y*-polarized laser light beams heterodyne with each other at the InGaAs photodetector (DSC50S, Discovery Semiconductors, Inc.), producing a radio-frequency beat note at 1.74 GHz. A polarizer and a polarization controller were used to maximize the beat signal. We amplified the laser output from 0.5 mW to 20 mW with an erbium-doped fiber amplifier (specialized at Beogold Technology, China) to suppress the shot noise at the photodetector. We then measured the beat signal using an electrical spectrum analyzer with a resolution of 10 kHz. The measured spectrum in Fig. S1c presents two sidebands with a frequency offset of 1.7 MHz due to laser relaxation oscillation, one of the prominent types of intensity noise of fiber lasers.

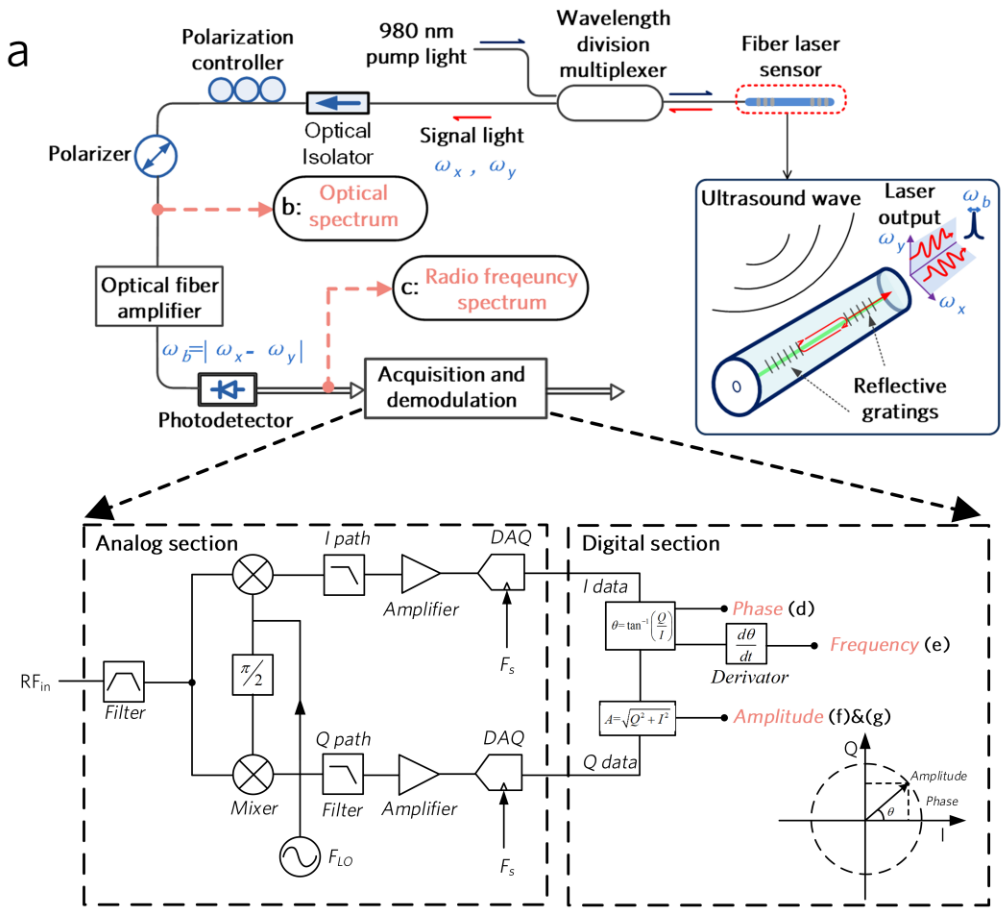

(to be continued)

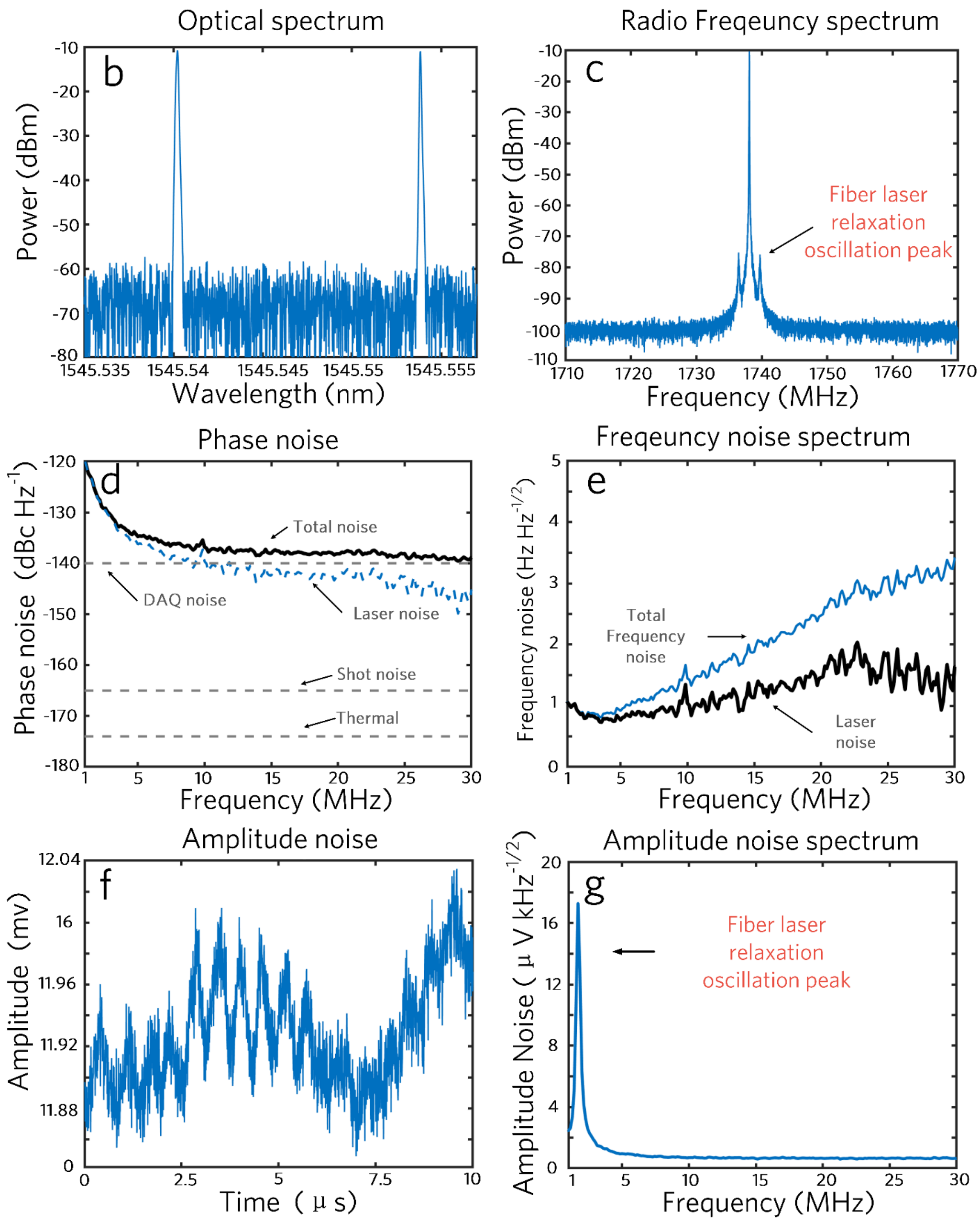

Supplementary Fig. S1. Schematic and noise characterization of the heterodyne laser-based sensing system. (a) Configuration of the sensing system. Insets: Ultrasound sensor and frequency demodulator. (b) Measured optical spectrum of the laser output. (c) Measured radio-frequency spectrum of the heterodyne signal. (d) Phase and (e) frequency noise spectra of the heterodyne signal. (f) Extracted time trace of amplitude fluctuation, and (g) its noise spectrum. The measured results in (b), (f) and (g) show noticeable amplitude fluctuations induced by laser relaxation oscillation at 1.7 MHz. However, this noise was not coupled into frequency demodulation, as shown in (d) and (e). We have marked the ports where the results in (b) to (g) were measured in (a).

We performed I/Q frequency demodulation by using a vectorial signal transmitter (5646R, NI), as illustrated in the inset of Fig. S1a. The incoming radio-frequency signal was mixed with a local oscillator with a working frequency close to ω_b in the analog section to downshift the carrier frequency to approximately 100 MHz. The signal was then split into in-phase (I) and quadrature-phase (Q) components with a 90-degree offset, which were separately digitized with a field-programmable gate array (FPGA) after filtering and amplification. We acquired the phase of the signal θ by calculating the arctangent of the ratio between I and Q data via θ=arctan(I/Q). Figure S1d shows the phase noise spectrum acquired by measuring the beat signal with the I/Q demodulator. The noise power density slowly decreases from approximately -130 dBc/Hz at 3 MHz to -140 dBc/Hz at 30 MHz. We then measured the noise after turning off the laser and found that its noise level is at approximately -140 dBm/Hz (or a -140 dBc/Hz dynamic range). By subtracting the total noise by the data acquisition (DAQ) noise, we can obtain the noise of the laser light after optical amplification, as shown in Fig. S1d. The average power density is approximately -140 dBc/Hz, and it has a descending profile with frequency. Figure S1d shows that the laser noise dominates over 1 to 10 MHz and becomes the secondary noise contribution over 10 to 30 MHz. The contributions of laser noise and the EDFA can be written together as [1]

$$N_{\text{sig}-\text{sp}} \approx -155.9\text{dBc/Hz} + NF + 19 - 20\log(i_{dc}) \tag{S-1}$$

We boosted the optical intensity to approach the saturation limit at the photodetector, yielding a photocurrent of i_{dc}=10 mA. The calculated $N_{\text{sig-sp}}$ is approximately -141 dBc/Hz with a noise figure NF=4 dB, which agrees with the measured result.

Additionally, the thermal noise N_{oth} and shot noise N_{shot} at the photodetector can be expressed as [1]

$$N_{\text{oth}} \approx k_{\text{B}}T \approx -174\ [\text{dBm/Hz}] \tag{S-2a}$$

$$N_{\text{shot}} \approx 2eI_{\text{dc}}Z_{\text{out}} \approx -169\ [\text{dBm/Hz}] + 10\log\,(i_{dc}[\text{mA}]) + 2H_{pd}[\text{dB}] \tag{S-2b}$$

where $i_{\text{dc}} = I_0 \cdot H_{\text{pd}}$, with $H_{\text{pd}} \approx 0.6\sim0.8$ A/W being the optical-to-electrical transduction coefficient, and the corresponding RNs can be expressed as

$$N_{\text{oth}} \approx \frac{k_{\text{B}}T}{i_{\text{dc}}^2 Z_{\text{out}}} \approx -155\ [\text{dBc/Hz}] - 20\log(i_{dc}[\text{mA}])\ \ (matched\ 50\Omega\ load) \tag{S-3a}$$

$$N_{\text{shot}} \approx \frac{2e}{i_{\text{dc}}Z_{\text{out}}} \approx -155\ [\text{dBc/Hz}] - 10\log(i_{\text{dc}}[\text{mA}]) \tag{S-3b}$$

where e denotes the elementary charge. The calculated values are $RIN_{\text{oth}} = -175$ dBc/Hz and $N_{\text{shot}} = -165$ dBc/Hz. In comparison, the contribution of the photodetector to the noise is very small and was neglected.

The frequency of the beat signal was reconstructed by applying a first-order time derivative to the phase data. Therefore, the I/Q frequency demodulator works like a differential filter, and the resultant frequency noise spectrum can be expressed as

$$n_{\text{f}} = \Omega \cdot N^{-\frac{1}{2}}\ [\text{Hz} \cdot \text{Hz}^{-1/2}] \tag{S-4}$$

where Ω denotes the ultrasound angular frequency, and N denotes the overall noise. Figure S1e shows the frequency noise spectrum. Due to the proportional frequency dependence, the frequency noise spectrum has an approximately linear variation from 1 Hz·Hz$^{-1/2}$ at 3 MHz to 3.5 Hz·Hz$^{-1/2}$ at 30 MHz. This means that the sensing system can offer an extremely high resolution in measuring the acoustically induced frequency modulation of 193-THz laser light. This single-longitudinal-mode laser can be considered a very silent light source, despite the 4 dB additional noise from the optical amplifier.

To evaluate the effect of laser relaxation oscillation, we extracted the amplitude of the beat signal with $A = \sqrt{I^2 + Q^2}$. Its time trace in Fig. 1f shows a noticeable periodic intensity fluctuation, which causes a peak in the intensity noise spectrum (Fig. 1g). However, this peak was not visible in the phase or frequency noise spectrum because of the low coupling efficiency between the intensity noise and phase noise (1~3%) [2]. In addition, the residual transduced noise was eliminated via common-mode cancelation between the orthogonally polarized laser light beams. This comparison demonstrates that our sensing system is immune to intensity fluctuation. As a result, the ultrasound detection capability is only determined by the phase noise n_q. We can fully boost the sensitivity by G to the upper limit of a frequency measurement system.

Supplementary Note S2: Ultrasound response

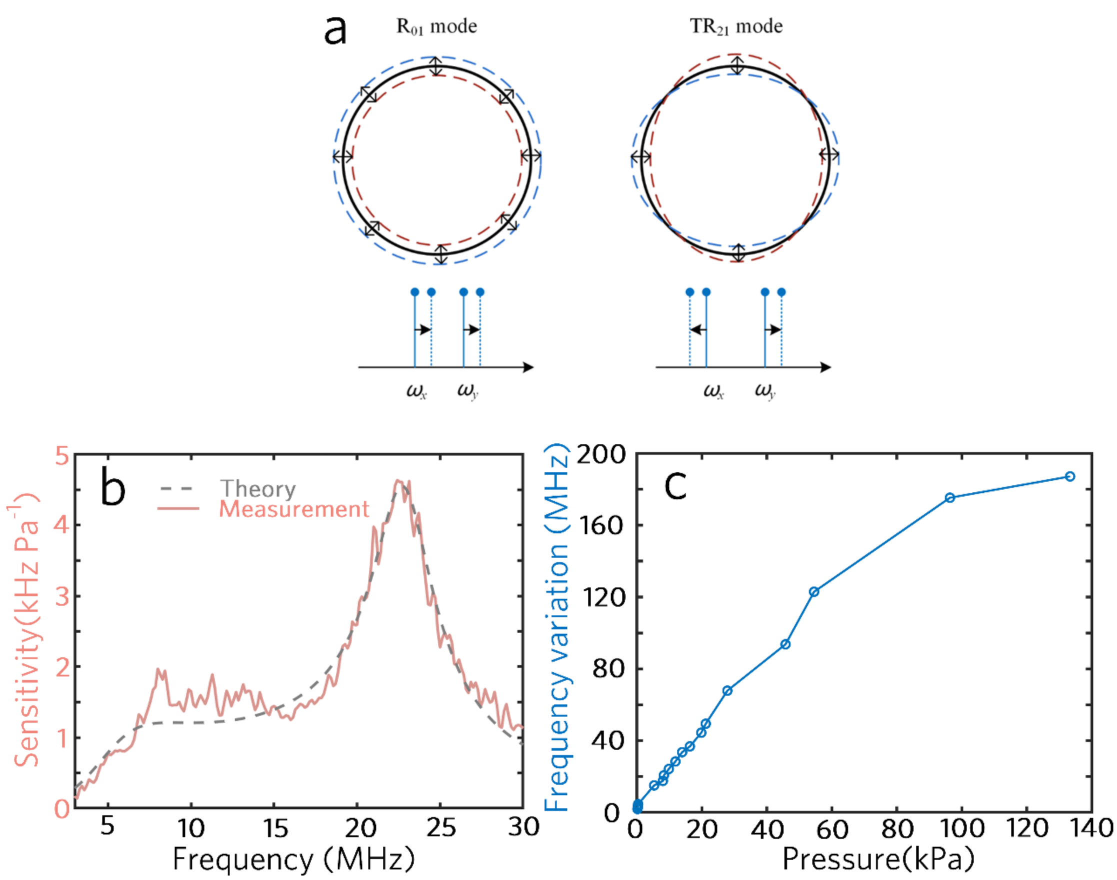

Supplementary Fig. S2. Ultrasound response. (a) R_{01} (l=0) and TR_{21} (l=2) vibrational modes. The former imposes homogenous stress on the fiber core and induces identical changes in the *x*- and *y*-polarized laser modes. This mode was excited by the incident ultrasound waves but not detectable by the heterodyne laser-based sensor. The latter causes differential stresses in the fiber core and can effectively shift the heterodyne frequency. (b) Calculated and measured ultrasound response. This response can be treated as the acoustic resonance of the silica fiber dampened by the surrounding water. The frequency response deviates from the Lorentz curve at frequencies lower than 15 MHz because of the significant difference between the acoustic wavelength and fiber diameter. (c) Measured ultrasonically induced frequency change as a function of applied acoustic pressure. The sensor has good linearity to approximately 60 kPa (or 120 MHz frequency variation).

A bare optical fiber can be treated as a homogeneous elastic cylinder in acoustics. Its transverse vibrational profiles can be calculated by solving the acoustic wave equations [3]. Briefly, the longitudinal and shear waves in the optical fiber can be respectively expressed by scalar and vectorial potentials written in the first-kind Bessel functions. The eigenfrequency (vibrational frequency), together with the displacement/stress profile of each mode, can be solved with the elastic parameters of silica density ρ_s=2240 kg·m^{-3}, longitudinal wave velocity c_L=5878 m/s and shear wave velocity c_S=3706 m/s. Only the l=0 and 2 azimuthal modes of the vibration can effectively induce optical path changes via the photoelastic effect. Figure S2a shows the R_{01} mode with l=0 and the TR_{21} mode with l=2. They are the first-radial-order modes for the l=0 and l=2 mode groups. The former mode, with an eigenfrequency of Ω_{R01} =2π×29 MHz, has an axially symmetric profile with isotropic stresses at the fiber core and induces identical frequency variations in the lasing frequencies ω_x and ω_y. Therefore, the beat frequency of the dual-polarization laser is not sensitive to this vibrational mode. The latter mode, with an eigenfrequency of Ω_{TR21}=2π×22 MHz, is a hybridization of longitudinal and shear waves. It compresses and stretches the fiber core in the two orthogonal directions. This vibration induces lasing frequency changes with equal amplitudes but opposite signs (or a π phase offset). As a result, the beat frequency has a doubled frequency modulation. The effect of fiber elongation is very weak and can be neglected here.

When subjected to an ultrasound wave, the optical fiber immersed in water (density: 1000 kg·m^{-3}, acoustic velocity: c_w=1480 m/s) vibrates in the individual transverse modes. The frequency spectrum of acoustic response $S(\Omega)$ can be calculated with an analytical solution [3]. Three linear equations are used to describe the acoustic interaction between the fiber and surrounding water. The strength of fiber vibration and the stresses, strains, and acoustic pressures can be solved for a specific incoming pressure wave and continuity boundary conditions. Figure S2b shows the calculated acoustic response $S(\Omega)$, which agrees with the measured result in Fig. 1h in the main manuscript. Alternatively, the sensor response can be understood based on a simplified acoustic resonance model. In this model, the optical fiber is considered an acoustic resonator, which is dampened by the surrounding medium. The ultrasound response can be expressed as

$$S(\Omega) = \frac{K}{\alpha(\Omega - \Omega_{TR21}) + i\delta} \tag{S-5}$$

where $K = \frac{1}{2} p_{44} \cdot n_0^2$, with p_{44}=-0.0695 being the effective strain-optic coefficient, and n_0=1.45 represents the refractive index of silica glass. The coefficient α=4.88×10^8/2π Pa·MHz^{-1} denotes the slope of frequency detuning, and δ=1.95×10^9 Pa represents the damping rate. For ultrasound frequencies below 10 MHz, the acoustic wavelength becomes significantly larger than the fiber diameter, the resonance effect is dramatically weakened, and the damping rate substantially decreases. As a result, the response curve deviates from a perfect Lorentz profile, yielding an asymmetric frequency response, as shown in Fig. S2b.

We also tested the linearity of the sensor by increasing the applied ultrasound pressure. Figure S2c shows the measured frequency shift as a function of applied acoustic pressure. The sensor suggests good linearity to approximately 60 kPa (or 120 MHz frequency variation), limited by the acquisition bandwidth (100 MHz for a 200 MHz acquisition rate).

Supplementary Note S3 A comparative study: Optical sensors versus piezoelectric sensors.

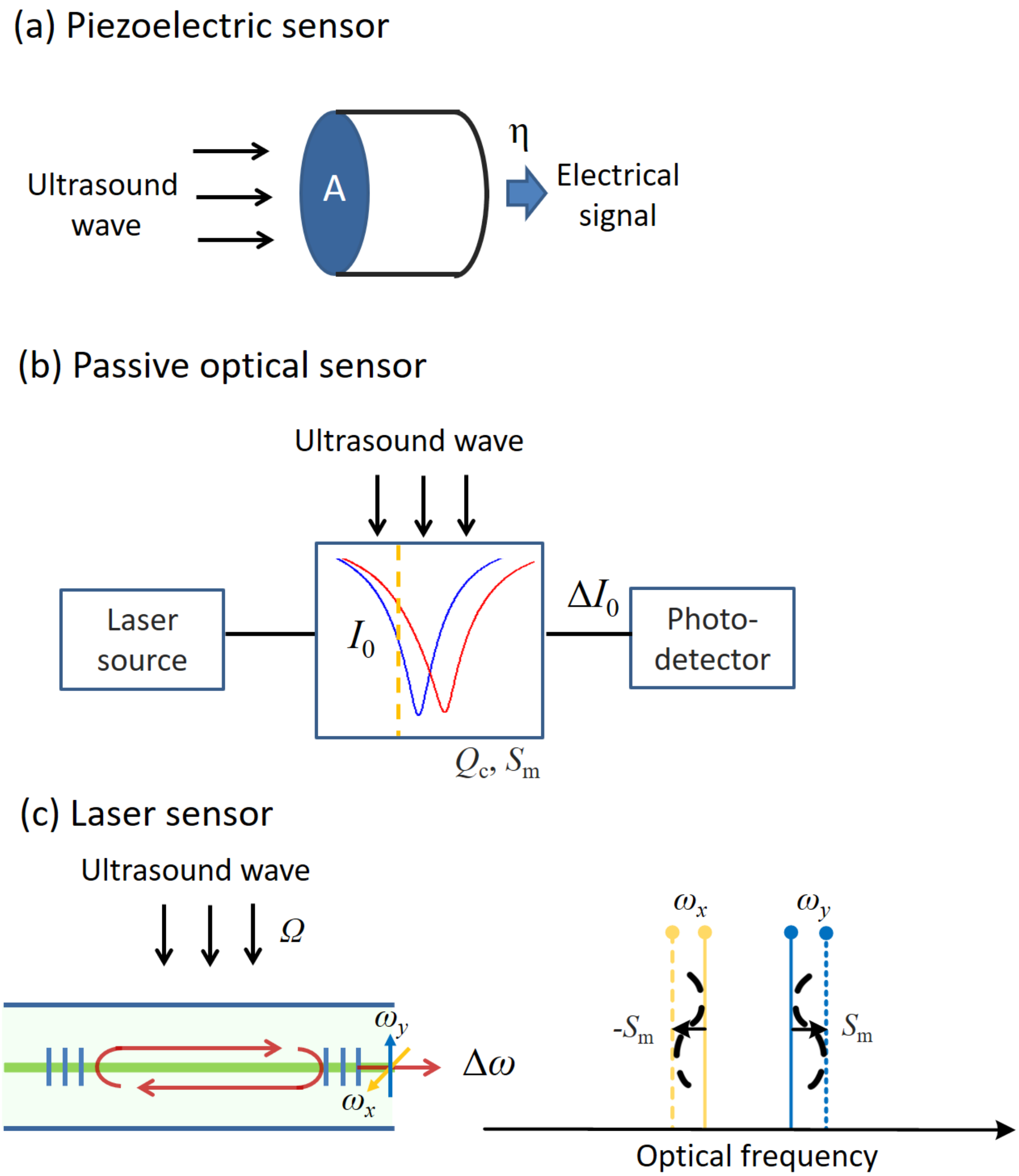

Supplementary Fig. S3. Difference in the working mechanism between piezoelectric and optical ultrasound sensors. (a) A piezoelectric sensor converts the acoustic energy into electrical energy with a ratio η. The sensitivity can be scaled up by the sensitive area A. (b) A resonator-based optical sensor transduces the acoustic pressure into a modulation in the intensity ΔI_0. The sensitivity is determined by S_m, which measures the sensor geometry modulation, and the quality factor Q_c, which amplifies the acoustic sensitivity. (c) The laser-based sensor has an output angular frequency at ω_0. The ultrasound wave at frequency Ω induces a frequency modulation and created two sidebands at $\omega_0 \pm \Omega$ with amplitudes $S_m G/2$, where $G = \omega_0/\Omega$ denotes the sensitivity gain factor.

In this note, we investigate the different mechanisms between piezoelectric and optical detection by examining the acoustic-to-electric energy transduction.

A. Piezoelectric sensors

A piezoelectric sensor partially converts the acoustic energy of an exerted pressure wave into electrical energy (Fig. S3a). The acoustic response in terms of electrical energy can be expressed as

$$R_{\mathrm{pe}} = \int_A p^2(x,y,z)\mathrm{d}A \cdot \frac{\eta_{\mathrm{pe}}}{Z_{\mathrm{a}}} \tag{S-6}$$

where $p(x,y,z)$ represents the complex amplitude of the pressure wave at a designated position (x,y,z), A denotes the acoustically sensitive area, η_{pe} is the acoustic-to-electric conversion efficiency, and $Z_{\mathrm{a}} = 1.5 \times 10^6$ Rayls is the acoustic impedance of the medium. In a focused manner, Eq. (S-6) can be simplified as $R_{pe} = E_a \cdot \eta_{\mathrm{pe}}$, where $E_a = \frac{p^2 \cdot A}{Z_a}$ represents the incident acoustic energy. The transduction ratio is relatively low, with η_{pe}=0.001 to 0.01. The detection sensitivity can be scaled up by increasing the ultrasonically sensitive area A (or acoustic numerical aperture), but a bulky ultrasound sensor is not suitable for endoscopic applications.

B. Passive optical sensors

Optical sensors do not induce energy conversion but modulate the light in an optical-to-electrical system. A typical photonic link consists of a laser source, a photodetector, and the intermediate section, which includes transmission lines, filters, and/or modulators. The optical sensor acts as one of the constructive parts. For example, ultrasound modulation of a passive optical sensor induces a resonant frequency change and modulates the intensity of the transmitted light (Fig. S3b).

A probe laser light is injected into the optical resonator for signal interrogation. Its wavelength is tuned to the quadrature point with the maximum spectral slope. The resonant spectrum acts as an edge filter with a slope $\frac{1}{\omega_{\mathrm{m}}} = \frac{Q_c}{\omega_{\mathrm{o}}}$ and translate the resonance shift into an intensity change $\frac{S_{\mathrm{m}} \cdot \omega_{\mathrm{o}}}{\omega_{\mathrm{m}}}$, where Q_{c} denotes the physical quality factor of the resonator. Notably, the edge filter also translates quadrature-phase noise component n_{q} to an intensity noise $\frac{n_q \Omega}{\omega_m}$. Now apply a monochromatic ultrasound wave $p(t) = p_0 \cos(\Omega t)$ at the sensor, the resonance frequency shifts by $\Delta\omega = p_0 S_{\mathrm{m}} \omega_0 \cos(\Omega t)$. The output signal after transmitting the edge filter can be expressed by

$$v = v_o(1 + S_{\mathrm{m}} Q_c \cos(\Omega t) + n_{\mathrm{q}} G / Q_c + n_{\mathrm{i}}) \tag{S-7}$$

Here we have the intensity of the transmitted light $I_0 = v_o^2$, the transduced electric energy is $E_t = (I_0 \cdot Q_c \cdot S_m \cdot H)^2 \cdot R$, where H=0.6~0.8 A/W denotes the optical-to-electric conversion coefficient of the photodetector and R is the resistor at the receiving end. As a result, the acoustic-to-electric transduction ratio can write as

$$\eta_{\mathrm{p}} = \frac{E_t}{E_a} = \frac{(I_0 \cdot Q_c \cdot S_m \cdot H)^2 \cdot R}{\frac{A}{Z_{\mathrm{a}}}} \tag{S-8}$$

C. Optical heterodyne detection

For laser sensors (Fig. S3c), the ultrasound wave induces a frequency modulation $\Delta\omega = p_0 S_{\mathrm{m}} \omega_0 \cos(\Omega \mathrm{t})$ in the laser light, which is identical with the passive resonator. The heterodyne signal can be expressed as

$$x(t) = A_b cos[\omega_b t + \theta(t)] \tag{S-9}$$

where $\theta(t) = \omega_o \cdot S_m \int p(t)dt,$ and A_b is the amplitude of the heterodyne signal, which is associated with the optical intensity as $A_b^2 = (I_0 H)^2 \cdot R$. Base on Eqs. (1), we have

$$X(\Omega) \approx A_b \exp{(i\omega_b t)} \left[1 + i p_0 S_{\mathrm{m}} \frac{\omega_0}{\Omega} \sin(\Omega \mathrm{t})\right], \tag{S-10}$$

where $\omega_b = \left|\omega_x - \omega_y\right|$. After demodulation, the carrier frequency ω_b shifts to *dc*, and the frequency modulation is converted into a single-sideband signal. Ignoring the *dc* component, Eq. (S-11) can be simplified to

$$X(\Omega) = \sqrt[2]{E_t(\Omega)} = A_b \frac{\omega_o \cdot S_m}{\Omega} \sin(\Omega \mathrm{t}) \tag{S-11}$$

The transduced electric energy is $E_t = (I_0 \cdot G \cdot S_m \cdot H)^2 \cdot R$; here, the optical gain factor is defined as $G = \frac{\omega_o}{\Omega}$. As a result, the acoustic-to-electric transduction ratio for the fiber laser sensor can be expressed as

$$\eta_{\mathrm{o}} = \frac{E_t}{E_a} = \frac{(I_0 \cdot G \cdot S_{\mathrm{m}} \cdot H)^2 \cdot R}{\frac{A}{Z_{\mathrm{a}}}} \tag{S-12}$$

The similar expression of η_{o} in Eqs. (S-8) and (S-12) suggest that optical sensors, both passive and laser sensors, can significantly amplify the energy transduction. The difference lies in the expression of the quality factor in that Q_{f} has a frequency dependency. It has a value of ~2×10^7 at 10 MHz and ~1×10^7 at 20 MHz. Table S1 lists the calculated η_{o} of some representative optical sensors based on Eqs. (S-8) and (S-12). For simplicity, we assume that the value of the term $(I_0 H)^2 \cdot R$ is 1 mW, which is typical for an undersaturated photodetector. We found that their values can be significantly higher than 1, while piezoelectric sensors have a typical η_{pe} of 0.001 to 0.01. This explains why small-sized optical sensors can provide a detection sensitivity comparable to that of a focused piezoelectric sensor.

Based on the above analysis, we found that the passive optical sensors are limited by both amplitude and frequency fluctuations, with a noise power $n = n_i + n_q \frac{\Omega}{\omega_{\mathrm{m}}}$. The corresponding NEPD can be expressed as

$$NEPD_{\mathrm{p}} = \left(\frac{n_i}{Q_c} + \frac{n_q}{G}\right) \cdot \frac{1}{S_{\mathrm{m}}} \tag{S-13}$$

Assume $n_{\mathrm{i}}=n_{\mathrm{q}}=n$, which hold for many laser sources, it can further write as

$$NEPD_{\mathrm{p}} = \frac{n}{S_{\mathrm{m}} G_{\mathrm{eq}}} \tag{S-14}$$

where G_{eq} is the equivalent gain factor defined by $\frac{1}{G_{\mathrm{eq}}} = \frac{1}{Q_c} + \frac{1}{G}$. The quality factor Q_{c} of a resonator-based sensor ranges from 10^3 to 10^6, as listed in Tab. S1. In contrast, the gain factor G has a typical value of ~2×10^7 at 10 MHz. As a result, we have $G_{\mathrm{eq}} \cong Q_{\mathrm{c}}$ for most cases, and the laser sensor can have a much higher sensitivity gain than the passive one.

Figure S4 plots the sensor dimensions and NEPDs of the piezoelectric and optical sensors listed in Tab. S1, which suggests that optical sensors can have smaller sizes and high sensitivities. As a result, optical sensors are more favorable for space-constrained imaging applications, including photoacoustic endoscopy.

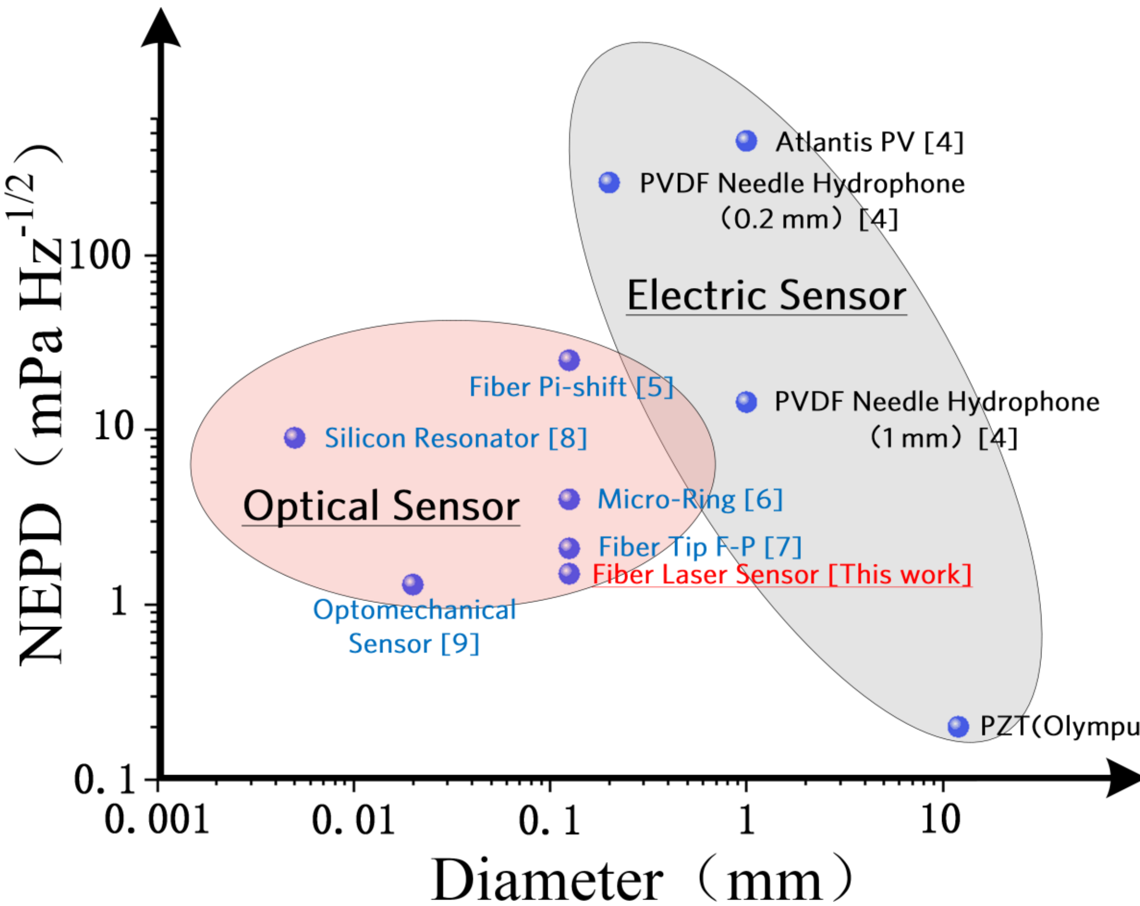

Supplementary Fig. S4. NEPDs of piezoelectric and optical ultrasound sensors versus diameter. Piezoelectric sensors degrade in sensitivity with decreasing sensor size. In contrast, optical sensors can offer sufficiently high sensitivities for hemodynamic imaging with sub-mm sizes and are suitable candidates for endoscopic imaging. Dashed line: Ideal relation between the NEPD and sensor diameter of piezoelectric sensors.

Supplementary Note S4: Error analysis of sO_2 measurement.

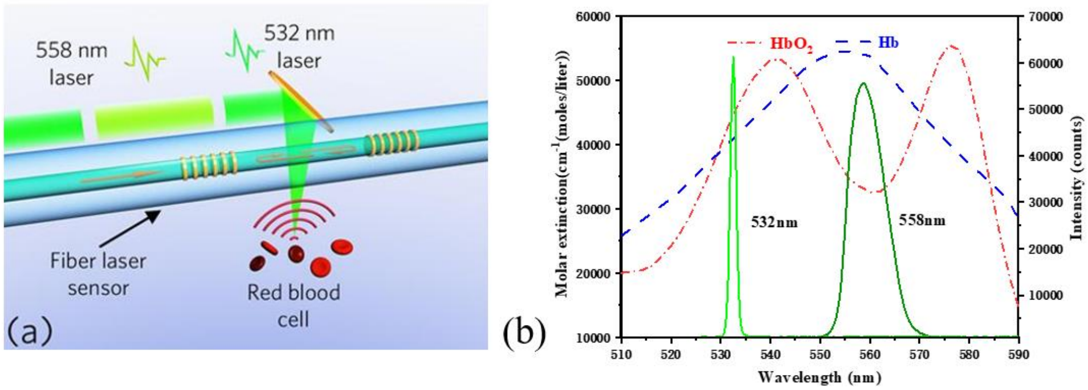

Supplementary Fig. S5. Photoacoustic measurement of sO_2. (a) Schematic of the experimental setup. The heterodyne laser-based sensor detects photoacoustic signals induced by the absorption of dual-color laser pulses. sO_2 can be calculated based on the Hb/HbO_2 difference in the absorption coefficient at the two wavelengths. (b) Optical absorption spectra of oxy- and deoxygenated hemoglobin (dashed curves), and optical spectrum of the dual-wavelength laser source in the experiment. The 558-nm component is the second-order Stokes wave due to the stimulated Raman scattering in a pure-silica-core optical fiber.

In biological and medical sciences, the oxygen saturation (sO_2), the percentage of oxygenated hemoglobin with respect to total hemoglobin, is defined as:

$$sO_2 = \frac{C_{HbO_2}}{C_{HbO_2}+C_{Hb}} \tag{S-15}$$

where C_{HbO_2} and C_{Hb} denote the concentrations of oxy- and deoxygenated hemoglobin (HbO_2 and Hb). Photoacoustic measurement of sO_2 takes advantage of the different absorption spectra between HbO_2 and Hb (Fig. S5). Supposing that the laser spot size at a biological absorber is much smaller than the ultrasound wavelength, the excited photoacoustic wave strength is almost proportional to the absorption coefficient. Thus, by using multiple wavelength excitation, the spectrum of the measured hemoglobin can be known, and sO_2 can be calculated via spectral unmixing. Practically, a dual-wavelength laser source is used for subsequent photoacoustic excitation. The excited photoacoustic signals are expressed as

$$PA_1 = I_1 \cdot \mu_1^{HbO_2} \cdot C^{HbO_2} + I_1 \cdot \mu_1^{Hb} \cdot C^{Hb} \tag{S-16a}$$

$$PA_2 = I_2 \cdot \mu_2^{HbO_2} \cdot C^{HbO_2} + I_2 \cdot \mu_2^{Hb} \cdot C^{Hb} \tag{S-16b}$$

where μ denotes the absorption coefficient at each wavelength, C represents the molecular hemoglobin concentration, and I is the optical fluence. For simplicity, we assume that the optical fluences are identical at each wavelength.

Based on Eq. (S-16), we can calculate sO_2 with measured photoacoustic signals based on

$$sO_2 = \frac{\frac{PA_2}{PA_1}\cdot\mu_1^{Hb} - \mu_2^{Hb}}{\frac{PA_2}{PA_1}\cdot\Delta\mu_1 - \Delta\mu_2} \tag{S-17}$$

where $\Delta\mu_{1,2} = \mu_{1,2}^{Hb} - \mu_{1,2}^{HbO_2}$ is the Hb/HbO_2 difference in the absorption coefficient at each wavelength. The measured photoacoustic strength has an error around the actual value in realworld measurements. This error can be transduced to sO_2 quantification, which can be estimated by calculating the first-order derivation of Eq. (S-17), expressed as

$$\delta sO_2 = \frac{|\Delta\mu_1 \cdot \mu_2^{Hb} - \Delta\mu_2 \cdot \mu_1^{Hb}|}{\left(\frac{PA_2}{PA_1} \cdot \Delta\mu_1 - \Delta\mu_2\right)^2} \cdot \left(\frac{1}{PA_1} + \frac{PA_2}{PA_1^2}\right) \cdot \delta PA \qquad \text{(S-18)}$$

Here, we have assumed that the uncorrelated errors have identical values $\delta PA_1 = \delta PA_2 = \delta PA$. Eq. (S-18) can be further expressed as

$$\delta sO_2 \cong \frac{2|\Delta\mu_1 \cdot \mu_2^{Hb} - \Delta\mu_2 \cdot \mu_1^{Hb}|}{(\Delta\mu_1 - \Delta\mu_2)^2} \cdot \frac{1}{\mathrm{SNR}} \qquad \text{(S-19)}$$

where the signal-to-noise ratio $\mathrm{SNR} = \frac{PA_{1,2}}{\delta PA}$, and we ignore the difference between PA_1 and PA_2 for simplicity. We used a 532- and 558-nm dual-wavelength laser for photoacoustic excitation in the experiment. Substituting μ_1^{Hb}=40584, μ_2^{Hb} = 54164, $\mu_1^{HbO_2}$ = 43876, and $\mu_2^{HbO_2}$ = 33456 ($cm^{-1} \cdot mole^{-1}$) into Eq. (S-19), we find that the noise is amplified by a factor of four in the transduction. As a result, quantitative assessment of sO_2 demands high SNR of the photoacoustic measurement. For example, sO_2 measurement with less than 10% error (to distinguish arteries from veins) demands an SNR above 20 dB, based on Eq. (S-19).

Supplementary Note S5: Photoacoustic endoscopy.

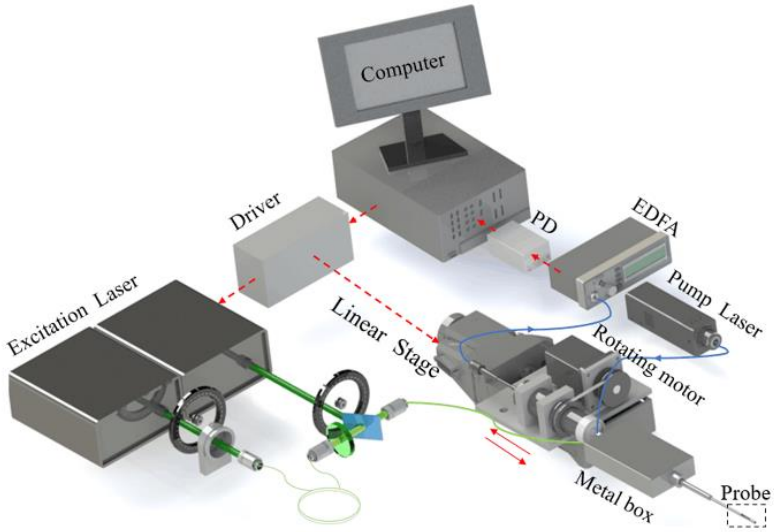

Supplementary Fig. S6. Experimental setup of photoacoustic endoscopy. The probe delivers laser pulses from the dual-color laser, focuses the laser beam on biological tissue, and detects the photoacoustic signals. The photoacoustic probe is rotated to form a circular B-scan image. Multiple B-scan images obtained via pullback scanning are used to construct a full volumetric image. The laser pulses, photoacoustic detection, and mechanical scanning are synchronized.

Figure S6 shows the experimental setup of photoacoustic endoscopy. The system consists of a photoacoustic probe, a dual-wavelength laser source, mechanical scanners, a DAQ module, and control modules. The probe delivered the excitation light using a single-mode fiber and focused it through a graded-index (GRIN) lens. The fiber and the GRIN lens were sheathed with a quartz tube with an inner diameter of 0.3 mm and an outer diameter of 0.5 mm. We controlled the fiber-lens distance to adjust the focal length. Next, we sealed them using ultraviolet curable glue to block the outside deionized water. Subsequently, we used a 1-mm right-angle prism to deflect the focused laser beam perpendicular to the imaging sample. Together with the heterodyne laser-based sensor, all these components were encapsulated in a steel sheath. A 12 mm-by-2.5 mm window was opened on the side of the sheath to transmit the excitation light and the ultrasound waves. Notably, the probe was entirely immersed in deionized water for acoustic coupling.

The photoacoustic probe delivers a pair of dual-wavelength laser pulses into biological tissue, detects the optically induced ultrasound waves, and forms an A-line. Each A-line contains 800 points at a sampling rate of 140 MHz. We interleaved the 532- and 558-nm pulses by 2.3 μs to avoid overlapping the subsequent photoacoustic signals or inducing the Grueneisen relaxation effect. The probe was rotated back and forth using a rotation stage to form the B-scan. We used 2000 A-lines to create the B-scan image in Fig. 3, with a 0.11° step size. The B-scan rate was 1 Hz. Then, a linear stage pulled the probe back step-by-step to produce a three-dimensional image.

The pullback step was 16 μm, and the speed was ~15 μm/s. Finally, 2000 B-scan slices were acquired to form a C-scan. We used a control card (PXI-7852R, National Instruments) to synchronize the laser pulses, scanning stages, and data acquisition.

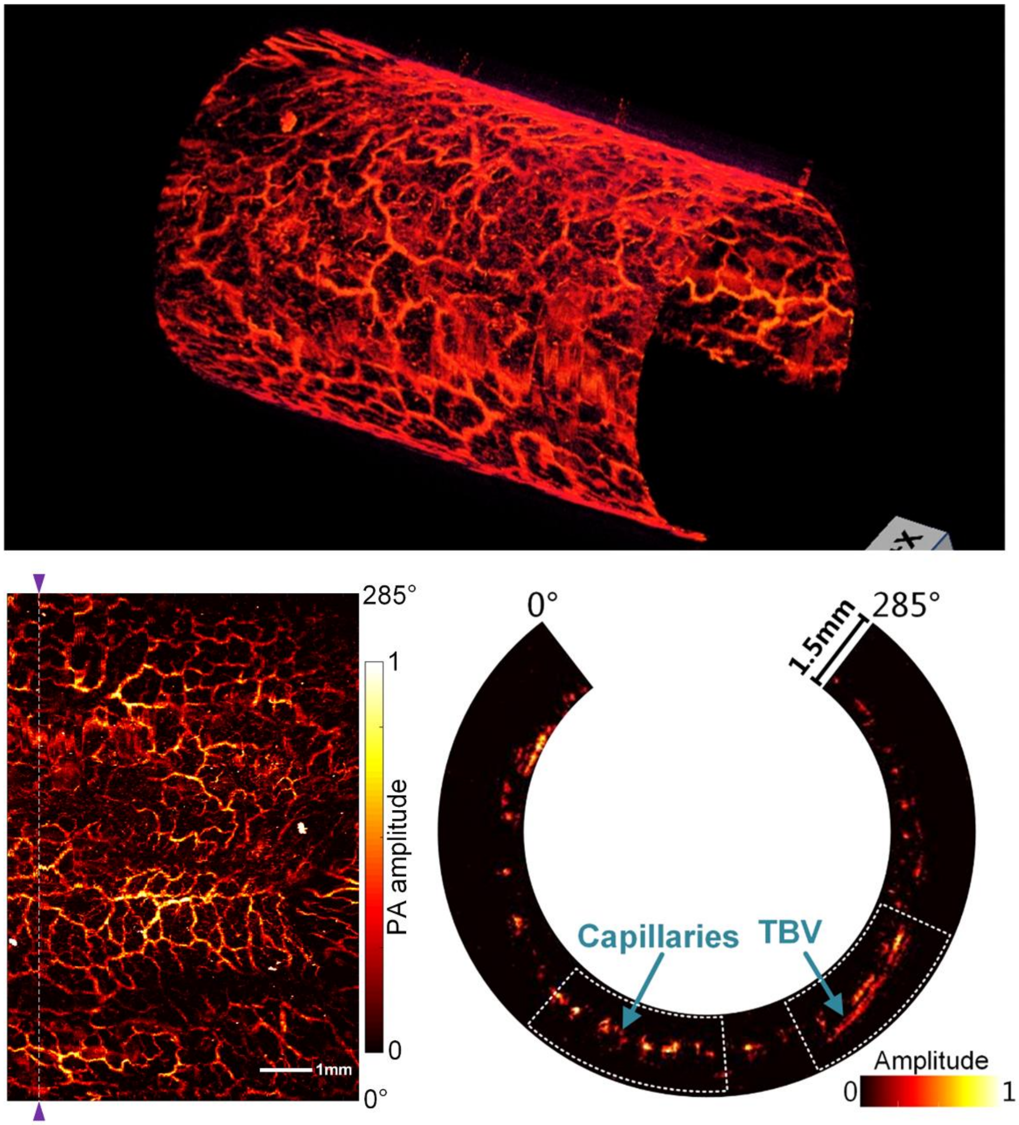

Supplementary Fig. S7. PAE imaging results. (a) 3D-rendered PAE image from a rat rectum. (b) Radial MAP image of (a). (c) Representative *x-y* slice at the location indicated by the arrow in (b). TBV: trunk blood vessel.

We used a polarization-maintaining fiber to guide the sensing light to minimize the rotation-induced polarization fluctuation. A WDM and a polarizer were encapsulated in a metal box and rotated with the probe. An optical slip ring was used to connect the box output with the photodetector. We tested the stability of the probe head during scanning in advance by repeatedly imaging a homogenous absorption simple in the curled state (black tape). The B-scan rate was 1 Hz, and the scanning lasted for over 30 minutes (1800 round trips or B-scans).

Figure S7 shows a typical *in vivo* 3D-rendered PAE image from a rat rectum (Sprague Dawley rat, female, 250 g) acquired at 532 nm. The reconstructed image in Fig. S7a exhibits an angular field of view of 285°. We maintained anesthesia with supplied 1.5–2.0% isoflurane during the imaging. Figure S7b shows the corresponding maximum amplitude projection (MAP) image. The right side of the radial MAP image corresponds to the anus, which shows the blood branches in the rectal wall. Figure S7c shows a selected B-scan image, demonstrating the trunk blood vessels (TBVs) and capillaries. We further achieved functional imaging by using dual-wavelength excitation and detection, as shown in Figs. 3 and 4 in the main text.

Table S1. Ultrasound sensitivities and energy transduction ratios of piezoelectric and optical sensors.

Sensor type	Optical sensors							Piezoelectric sensors	
	Microring resonator	Fabry–Perot cavity (planar)	Fabry–Perot cavity (fiber)	Optomechanical waveguide	Phase-shifted Bragg grating	Silicon nanoresonator	Laser sensor *(This work)*	Spherically focused piezoceramic	PVdF needle hydrophone
Quality factor* ($\times 10^6$)	0.14	0.0028	0.1	0.003	1.2	0.02	10 (at 20 MHz)	N. A.	N. A.
S_m ($\times 10^{-6}$ MPa^{-1})	130	90	100	19354	3.8	5	11	N. A.	N. A.
Sensing area A ($\times 10^{-3}$ mm^2)	0.32	6.4	0.2	0.32	2.7	0.0001	10	30000	1000
Transduction efficiency η (mm^{-2})	1553	0.015	750	15803	12	150	1815	0.01	0.001
NEPD (mPa·Hz$^{-1/2}$)	5.6	78	2.1	1.3	25	9	1.5	0.2	14.4

* Here, we list the value of the physical quality factor of the optical resonators Q_c for the former six works and G for the laser sensor, which are associated with the sensitivity gain in energy transduction.

References for Supplementary Materials

[1] Urick, V.J., K.J. Williams, and J.D. McKinney, *Fundamentals of microwave photonics*. 2015: John Wiley & Sons.

[2] Rønnekleiv, E., *Frequency and intensity noise of single frequency fiber Bragg grating lasers.* Optical Fiber Technology, 2001. **7**(3): p. 206-235.

[3] Liang, Y., Sun, H., Cheng, L., Jin, L., Guan, B.-O., *High spatiotemporal resolution optoacoustic sensing with photothermally induced acoustic vibrations in optical fibres*. Nature communications **12**, 1-10 (2021).

[4] Wissmeyer, G., et al., *Looking at sound: optoacoustics with all-optical ultrasound detection.* Light: Science & Applications, 2018. **7**(1): p. 1-16.

[5] Rosenthal, A., et al., *Sensitive interferometric detection of ultrasound for minimally invasive clinical imaging applications.* Laser & Photonics Reviews, 2014. **8**(3): p. 450-457.

[6] Zhang, C., et al., *Review of imprinted polymer microrings as ultrasound detectors: Design, fabrication, and characterization.* IEEE Sensors Journal, 2015. **15**(6): p. 3241-3248.

[7] Guggenheim, J.A., et al., *Ultrasensitive plano-concave optical microresonators for ultrasound sensing.* Nature Photonics, 2017. **11**(11): p. 714-719.

[8] Shnaiderman, R., et al., *A submicrometre silicon-on-insulator resonator for ultrasound detection.* Nature, 2020. **585**(7825): p. 372-378.

[9] Westerveld, W.J., et al., *Sensitive, small, broadband and scalable optomechanical ultrasound sensor in silicon photonics.* Nature Photonics, 2021. **15**(5): p. 341-345.